Multipartite nonlocality and topological quantum phase transitions in a spinless fermion quantum wire with uniform and incommensurate potentials

Zhao-Yu Sun,[1,*] Hai-Lin Huang,[1] Hui-Xin Wen,[1] Meng Li,[1] Xu Zhao,[1] Hong-Guang Cheng,[1] Duo Zhang,[1] and Bin Guo[2]
[1]*School of Electrical and Electronic Engineering, Wuhan Polytechnic University, Wuhan 430023, China*
[2]*Department of Physics, Wuhan University of Technology, Wuhan 430070, China*

(Received 20 May 2022; revised 2 August 2022; accepted 3 August 2022; published 15 August 2022)

Multipartite nonlocality and Bell-type inequalities are used to characterize topological quantum phase transitions (QPTs) in a spinless fermion quantum wire, where both uniform potentials and incommensurate potentials are considered. First, the nonlocality measures show clear signals at the critical points in both the uniform model and the incommensurate model. It indicates that these QPTs are accompanied by dramatic changes of multipartite quantum correlations in the ground states. Second, finite-size scaling analysis is carried out. In particular, in the incommensurate model where translation invariance is broken, with some rescaling techniques, we successfully establish the scaling formula in the large-L limit. Finally, the full phase diagram of the model with mixed potentials is figured out. We find a region which is featured with strong randomness in the large-L limit. The structure of this region is revealed by analyzing the energy spectrum, and an efficient approach to characterize this region is proposed.

DOI: 10.1103/PhysRevA.106.022208

I. INTRODUCTION

Quantum phase transitions (QPTs) are interesting phenomena in condensed matter physics [1]. They occur at zero temperature and are driven by quantum fluctuations. Consider a quantum system described by a Hamiltonian $\hat{H}(\lambda)$ with λ being the controlling parameter. As λ changes, the ground states of the system may change dramatically at some point $\lambda = \lambda_c$ and exhibit fundamentally different properties at the two sides of this point. Then we say that the system undergoes a QPT at the QPT point $\lambda = \lambda_c$. QPTs have been observed in various quantum systems, and the characterization of these QPTs is one of the most important topics in condensed matter physics [2,3].

QPTs may be accompanied by some general features, such as the breaking of symmetry [1]. Moreover, some QPTs can be characterized by local order parameters such as the average magnetization, while some QPTs need to be studied by nonlocal order parameters, such as the Chern numbers describing topological orders [4,5]. Recently, many concepts from the quantum information theory have been widely used to characterize QPTs in low-dimensional quantum lattices. For instance, Osterloh *et al.* have used the entanglement concurrence (a measure of two-qubit entanglement) to characterize the QPT in the transverse-field Ising chains [6]. Quantum fidelity and closely related quantities have also been used to characterize QPTs in many models [7]. Nevertheless, the biggest achievement in this field have been obtained by the entanglement entropy (a measure of bipartite entanglement) [8]. Entanglement entropy has not just deepened our understanding on low-dimensional quantum lattices, but also greatly promoted the development of the tensor-network algorithms in the field [9].

In some many-body quantum systems, *bipartite* quantum entanglement may not be sufficient to capture all the valuable information in the system [10–15]. Thereby, *multipartite* nonlocality—a measure of multipartite quantum correlations—and QPTs have been studied in various quantum lattices [16–26]. In the past ten years, great progress has been made in several aspects. First, as tensor-network algorithms are introduced into this field, the size of the system that can be handled has been extended from $n = 2, 3$ in early analytical research on several exactly soluble models [16–18,27] to rather large n in general quantum spin chains (such as transverse-field Ising chains, XY chains, spin ladders, and Kitaev chains) [22,24,26]. For instance, in the transverse-field Ising chains, it is found that the boundary effects on multipartite nonlocality increase steadily in the critical regions, and converge to a nonzero constant in noncritical regions [28]. Second, the scope of research has extended from traditional QPTs (which can be captured by local order parameters) to topological QPTs (which can be captured by non-local quantities) [17,29–31]. For instance, in the bond-alternating Heisenberg chains, multipartite nonlocality is observed in one phase and is absent in the other phase, and thus presents quite sharp signals for the topological QPT in the ground states of the model [31]. Third, with the help of matrix product operators and thermal-state tensor networks [32], the algorithms for calculating multipartite nonlocality has been generalized from zero-temperature ground states [22] to finite temperatures recently [26]. Fourth, these studies have covered not just one-dimensions (1D) lattices but also several high-dimensional lattices [25,33,34]. In particular, in some regions of the Lipkin-Meshkov-Glick (LMG) model, it is found that multipartite nonlocality can capture multipartite correlations

*Corresponding author: sunzhaoyu2020@whpu.edu.cn

[25] while the bipartite entanglement concurrence and the generalized global entanglement (another measure of many-body entanglement) fail [15]. It is worth mentioning that quite recently a transfer-matrix theory has been proposed to offer a general description about the finite-size scaling behavior of multipartite nonlocality in 1D translation-invariant quantum lattices [35].

These studies show unambiguously that multipartite nonlocality can reveal valuable information about quantum correlations and QPTs in various quantum lattices. Nevertheless, their limitations are also clear. In fact, most of these studies only considered (1) quantum spin models and (2) translation-invariant lattices. First, quantum spin models are magnetic models. However, in many important physical systems, some other models are involved and deserve further study. Second, translation invariance is indeed an important fundamental symmetry in many materials. Nevertheless, in some modern experiments such as in ultra-cold-atom experiments [36], incommensurate potentials can emerge naturally, where translation invariance is absent and a number of interesting phenomena are observed. Thereby, it shall be valuable to investigate the behavior of multipartite nonlocality in those quantum systems without translation invariance.

In this paper, we will investigate multipartite nonlocality in a spinless fermion quantum wire by considering both uniform potentials [37] and incommensurate potentials [38]. The model can undergo topological-type QPTs in the ground states, which cannot be characterized with local order parameters. The most exciting result of this paper is that the global nonlocality measure (defined on the wave functions of the entire lattice) and the partial nonlocality measure (defined on the reduced density matrices of subchains) can signal the QPTs in both the uniform model and the incommensurate model. Furthermore, we will analyze the full phase diagram of the models with mixed potentials. Especially, we find an interesting region which is featured with frequent level crossings and a multi-kink-point structure in the nonlocality curves. The mystery in this region will be revealed by analyzing the spectrum.

This paper is organized as follows. We will introduce the concepts of multipartite nonlocality and Bell-type inequalities in Sec. II. Models and the solutions will be introduced in Sec. III. The main results will be divided into four sections, i.e., Secs. IV to VII. A summary and some discussions can be found in Sec. VIII.

II. MULTIPARTITE NONLOCALITY AND BELL-TYPE INEQUALITIES

In this section, we will provide a concise introduction to multipartite nonlocality and Bell-type inequalities [12,13,39–43].

In n-site systems, the possible patterns of many-body correlations would be much more complex than in two-site systems. Let us take, for instance, a quantum model consisting of four sites a, b, c, and d. Suppose only a, b, and c share nonlocal correlations with each other; then we may label the model as $\{abc|d\}$. In Fig. 1, we have illustrated various patterns of multipartite correlations, from the local model $\{a|b|c|d\}$ which does not present any correlation to the model $\{abcd\}$ which presents the highest hierarchy of multipartite correlations.

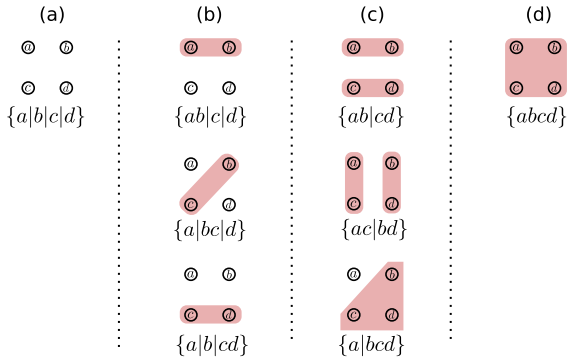

FIG. 1. Various patterns of multipartite correlations in n-site systems with $n = 4$. Circles denote the sites, and pink shadows denote regions in which the sites can share nonlocal correlations with each other. From panels (a) to (d), the *hierarchy* of the multipartite correlations increases gradually. The hierarchy of multipartite correlations can be characterized by Bell-type inequalities.

When n is rather large (i.e., $n \approx 10^2$ in condensed matters), it is expected that a *detailed* characterization of multipartite correlations in the form of $\{a|b|cde\ldots\}$ becomes both intractable and unnecessary. A slightly rough and feasible approach is to classify general n-site quantum states into various hierarchies according to the grouping number g [12]. For instance, we shall classify $\{a|b|c|d\}$ into the lowest hierarchy with a grouping number $g = 4$ [Fig. 1(a)]. Moreover, we can classify both $\{ab|c|d\}$ and $\{a|bc|d\}$ into a slightly higher hierarchy with $g = 3$ [Fig. 1(b)]. Furthermore, we can classify both $\{ab|cd\}$ and $\{a|bcd\}$ into a high hierarchy with $g = 2$ [Fig. 1(c)]. Finally, $\{abcd\}$ should be classified into the highest hierarchy with $g = 1$ [Fig. 1(d)]. It is clear that a model with a larger (smaller) grouping number g presents a lower (higher) hierarchy of multipartite correlations. Thereby, the grouping number g with $g \in \{1, 2, \ldots, n\}$ can offer a *rough* but still *informative* and *intuitive* characterization of multipartite correlations in n-site systems.

For an n-site quantum state $\hat{\rho}_n$, its grouping number g can be detected by Bell-type inequalities proposed by Mermin, Klyshko and Svetlichny *et al.* [44–46]. First of all, on each site, we can construct two local observables as

$$\hat{s}_i = \boldsymbol{a}_i \cdot \boldsymbol{\sigma}, \quad \hat{s}'_i = \boldsymbol{a}'_i \cdot \boldsymbol{\sigma}, \tag{1}$$

where $\boldsymbol{a}_i$ and $\boldsymbol{a}'_i$ are unit vectors in real space, and $\boldsymbol{\sigma} = (\hat{\sigma}^x, \hat{\sigma}^y, \hat{\sigma}^z)$ is the Pauli vector. Then, the n-site Mermin-Klyshko-Svetlichny operator $\hat{S}_n$ can be constructed recursively as [12,47]

$$\hat{S}_n = \tfrac{1}{2}\hat{S}_{n-1} \otimes (\hat{s}_n + \hat{s}'_n) + \tfrac{1}{2}\hat{S}'_{n-1} \otimes (\hat{s}_n - \hat{s}'_n). \tag{2}$$

The operator $\hat{S}'_{n-1}$ is given by exchanging all the $\boldsymbol{a}_i$ and $\boldsymbol{a}'_i$ in $\hat{S}_{n-1}$. It is clear that $\hat{S}_n$ depends upon a set of unit vectors $\underline{s} = \{\boldsymbol{a}_1, \boldsymbol{a}'_1, \boldsymbol{a}_2, \boldsymbol{a}'_2, \ldots, \boldsymbol{a}_n, \boldsymbol{a}'_n\}$.

Bancal *et al.* have proved that if the multipartite correlations in $\hat{\rho}_n$ can be reproduced by some models with a grouping number g, the following Bell-type inequalities should hold

[12]

$$\mathcal{S}_n = \begin{cases} \max_{\underline{s}} \mathrm{Tr}(\hat{\rho}_n \hat{S}_n) \leqslant 2^{\frac{n-g}{2}}, & \text{for n-g even,} \\ \max_{\underline{s}} \mathrm{Tr}(\hat{\rho}_n \hat{S}_n^{+}) \leqslant 2^{\frac{n-g}{2}}, & \text{for n-g odd,} \end{cases} \tag{3}$$

with $\hat{S}_n^{+} = (\hat{S}_n + \hat{S}_n')/\sqrt{2}$.

If the inequality is violated, we conclude that the grouping number of $\hat{\rho}_n$ is (*at most*) $g-1$. Thereby, these Bell-type inequalities offer us an approach to analyze the grouping number g (and consequently, the multipartite correlations) of the concerned quantum state. Moreover, multipartite correlations detected by the violation of Bell-type inequalities are usually called *multipartite nonlocality*. For instance, the lowest rank inequality is $\mathcal{S}_n \leqslant 2^{\frac{n-n}{2}} = 1$. If it is violated, the grouping number for $\hat{\rho}_n$ is (at most) $n-1$. Thus we can conclude that the state cannot be described by any local model; in other words, multipartite nonlocality is observed. The highest rank inequality is $\mathcal{S}_n \leqslant 2^{\frac{n-2}{2}}$. If it is violated, the grouping number of $\hat{\rho}_n$ would be (at most) $2-1$; in other words, we have $g=1$. Thus, we conclude that the state presents the highest hierarchy of multipartite nonlocality, i.e., genuine multipartite nonlocality. Generally speaking, a *larger* value of $\mathcal{S}_n$ would indicate that $\hat{\rho}_n$ has a *smaller* grouping number, and consequently, a *higher* hierarchy of multipartite nonlocality.

It needs mention that the inequalities in Eq. (3) are just a special family of Bell-type inequalities. There are some other Bell-type inequalities in the literature [44–46,48]. Thereby, the violation of these inequalities is just a *sufficient but not necessary* condition to identify the presence of multipartite nonlocality. Moreover, in condensed matter physics, we are usually not interested in the specific value of the grouping number g. Instead, we just want to establish some qualitative description about multipartite nonlocality in the concerned system. Thereby, in this paper we shall ignore the parity of $n-g$ in Eq. (3) and just consider the inequalities with an even $n-g$.

III. MODEL AND METHOD

A. Model

We will investigate a p-wave superconductor wire described by a 1D spinless fermion quantum model with an open boundary condition [37,38],

$$\begin{aligned} \hat{H} = &-\sum_{i=1}^{L-1} t(c_i^{\dagger} c_{i+1} + c_{i+1}^{\dagger} c_i) \\ &+ \sum_{i=1}^{L-1} \Delta(c_i c_{i+1} + c_{i+1}^{\dagger} c_i^{\dagger}) \\ &- \sum_{i=1}^{L} \mu_i c_i^{\dagger} c_i, \end{aligned} \tag{4}$$

where t is the uniform hopping amplitude, Δ denotes the p-wave pairing interaction, and μ_i is the chemical potential on site i. $t=1$ will be used as the unit of energy in this paper.

We will consider both uniform chemical potentials and incommensurate potentials, i.e.,

$$\mu_i = U_0 + \mu \cos(2\pi i\alpha), \tag{5}$$

where U_0 and u denote the strength of the uniform potentials and the incommensurate potentials, respectively, and $\alpha = (\sqrt{5}-1)/2$ is an irrational number. We will call it the *mixed-potential model* in this paper.

When $\mu = 0$, the model would be reduced to the *uniform model* studied in Ref. [37], with

$$\mu_i = U_0. \tag{6}$$

This uniform model has two quantum phases. For $U_0 < 2|t|$ with $\Delta \neq 0$, the model is in a topologically nontrivial superconducting (SC) phase, where Majorana bound states are present at the ends of the lattice. For $U_0 > 2|t|$, the model is in a topologically trivial localized phase, and the Majorana bound states are absent. The physical picture of this localized phase can be understood by considering $U_0 \to \infty$, where the ground state tends to be $|1, 1, 1, \ldots, 1\rangle$, i.e., a fully occupied state. A topological QPT occurs at $U_{0c} = 2|t|$.

When $U_0 = 0$, the mixed-potential model would be reduced to the *incommensurate model* studied in Ref. [38], with

$$\mu_i = \mu \cos(2\pi i\alpha). \tag{7}$$

This model also has two phases. When the strength μ of the incommensurate potential is weak enough, it is expected that the ground state is still in the topologically nontrivial SC phase with the edge Majorana fermions. When μ is large enough, the SC phase would be destroyed, and the model would be driven into a topologically trivial localized phase. The physical picture of this localized phase can be understood by considering $\mu \to \infty$, where the ground state tends to be a randomly occupied state $|1, 0, 0, \ldots, n_i, \ldots, 1, 0\rangle$, where the on-site occupation number n_i is given by

$$n_i = \begin{cases} 1, & \cos(2\pi i\alpha) > 0 \\ 0, & \cos(2\pi i\alpha) < 0 \end{cases}. \tag{8}$$

A topological QPT occurs at $\mu_c = 2(t+\Delta)$.

It is well known that with Jordan-Wigner transformations, the Hamiltonian in Eq. (4) can be mapped into the XY model with an (irrationally modulated) transverse field, i.e.,

$$\hat{H} = -\sum_i \left[J_x \hat{\sigma}_i^x \hat{\sigma}_{i+1}^x + J_y \hat{\sigma}_i^y \hat{\sigma}_{i+1}^y \right] + \sum_i h_i \hat{\sigma}_i^z \tag{9}$$

with $J_x = \frac{t+\Delta}{2}$, $J_y = \frac{t-\Delta}{2}$ and $h_i = \frac{\mu_i}{2}$. It has been pointed out that these nonlocal Jordan-Wigner transformations can change the physical properties of the models [37]. For instance, Shan *et al.* have shown that under a weak random perturbation, a spinless fermion wire and its corresponding Ising chain behave quite differently [49]. Moreover, by comparing two-site reduced density matrices, an in-depth analysis about the difference between the spinless fermion wire and its corresponding spin chains have been carried out in Ref. [50]. Since Eqs. (4) and (9) are not physically equivalent, in this paper we always consider Eq. (4) in our numerical simulations so to avoid possible misunderstandings.

The model has a Z_2 symmetry [51], where the corresponding good quantum number is the fermion parity P, i.e., particle number modulo 2. We will use $|\psi_0\rangle$ and $|\psi_1\rangle$ to denote the lowest lying state in the $P=0$ sector and $P=1$ sector, respectively. In the uniform model with an even finite L, $|\psi_0\rangle$

is the true ground state and $|\psi_1\rangle$ is the first-excited state.[1] In the incommensurate model, as we will show, the multipartite nonlocality measures for $|\psi_0\rangle$ and $|\psi_1\rangle$ become approximately equal to each other for any μ. Thereby, the results reported in this paper just correspond to $|\psi_0\rangle$, when there is no clear statement.

Our research are organized as follows. The uniform model with the p-wave pairing interaction $\Delta = 1$ will be discussed in Sec. IV. The incommensurate model with $\Delta = 1$ will be discussed in Sec. V. The interplay between Δ and chemical potentials will be studied in Sec. VI. Finally, the full phase diagram of the mixed-potential model will be reported in Sec. VII.

B. Method

1. Calculation of energy spectrum

First of all, the Hamiltonian in Eq. (4) is a standard quadratic form in terms of Fermi operators and can be exactly diagonalized into

$$\hat{H} = \sum_n \Lambda_n \eta_n^\dagger \eta_n + \text{const.} \tag{10}$$

Explicitly, by defining a symmetric $L \times L$ square matrix A as [52]

$$A_{ij} = \mu_i \delta_{i,j} - t\delta_{i+1,j} - t\delta_{i-1,j}, \tag{11}$$

and an antisymmetric $L \times L$ square matrix B as

$$B_{ij} = \Delta\delta_{i+1,j} - \Delta\delta_{i-1,j}, \tag{12}$$

Lieb *et al.* have shown that Λ_n^2 are just the eigenvalues of the matrix $(A-B)(A+B)$. Suppose we demand $0 \leqslant \Lambda_1 \leqslant \Lambda_2 \ldots$; then the full spectrum of the model is given by $\pm\Lambda_n$, and the ground state corresponds to the state with all negative-energy modes filled. The energy gap ΔE is just determined by the spectrum, i.e., $\Delta E = 2\Lambda_1$.

2. Two-site density matrices

For the uniform model in Eq. (6), the reduced density matrices $\hat{\rho}_2$ for two nearest neighboring sites i and $i+1$ can been figured out analytically [50,53]. Because of the symmetry of the model, $\hat{\rho}_2$ shall take the following form,

$$\hat{\rho}_2 = \begin{pmatrix} 1+2x+y & & & m \\ & 1-y & n & \\ & n & 1-y & \\ m & & & 1-2x+y \end{pmatrix}, \tag{13}$$

with $x = \langle\hat{\sigma}_i^z\rangle$, $y = \langle\hat{\sigma}_i^z\hat{\sigma}_{i+1}^z\rangle$, $m = \langle\hat{\sigma}_i^-\hat{\sigma}_{i+1}^-\rangle$, and $n = \langle\hat{\sigma}_i^+\hat{\sigma}_{i+1}^-\rangle$. These quantities can be figured out easily [50,52,53], and we have provided the corresponding formula in the Appendix of this paper.

3. Ground-state wave functions

In order to investigate multipartite nonlocality in one-dimensional chains, it is necessary for us to consider long subchains with $n > 2$. Therefore, numerical algorithms shall be used, such as the density matrix normalization group (DMRG) algorithm. Efficient implementations for DMRG can be found in many open-source packages, such as the ALPS package [51], the Itensor library [54], and the Matrix-Product Toolkit [55]. In this paper, we will use the ALPS package to express the ground states into matrix product states [51]. [In order to verify the modeling and numerical process in ALPS, we have independently calculated the ground state of the model (with $L = 3, 4$) by ALPS and an exact diagonalization code, and carefully checked the wave functions. The reliability of the numerical result of ALPS is confirmed unambiguously.] In ALPS calculations, we set the maximal bond dimension as $\chi = 200$, and we always sweep the lattices for 50–200 times so as to ensure the convergence of the wave functions. Moreover, Z_2 symmetry is adopted so as to improve the accuracy of the wave functions.

4. Analytical expression for $\mathcal{S}_2$

In the second step, we need to calculate the nonlocality measure $\mathcal{S}_n$ for a given $\hat{\rho}_n$. For a two-qubit state $\hat{\rho}_2$, $\mathcal{S}_2$ can be solved exactly by Horodeckis' formula [56]. To proceed, we shall construct a 3×3 matrix Q as $Q_{ij}(\hat{\rho}_2) = \text{tr}[\hat{\rho}_2 \cdot \hat{\sigma}_i \otimes \hat{\sigma}_j]$, with $i, j = x, y, z$. Then $\mathcal{S}_2$ is just given by

$$\mathcal{S}_2 = \sqrt{\lambda_1 + \lambda_2}, \tag{14}$$

with λ_1 and λ_2 being the two largest eigenvalues of a 3×3 matrix $Q^{\text{T}}Q$.

For density matrices in the form of Eq. (13), one can easily find that Q is a diagonal matrix,

$$Q = \begin{pmatrix} 2(m+n) & & \\ & 2(n-m) & \\ & & 4y \end{pmatrix}. \tag{15}$$

Consequently, λ_1 and λ_2 are the two largest numbers in $\{4(m+n)^2, 4(n-m)^2, 16y^2\}$.

5. Numerical optimization of $\mathcal{S}_n$

For a general quantum state $\hat{\rho}_n$ with $n > 2$, there is no analytical solution. Thus, we need to carry out a multivariable optimization with respect to $2n$ unit vectors $\{\ldots \boldsymbol{a}_k, \boldsymbol{b}_k \ldots\}$. A numerically efficient approach to solve the problem is the two-site update algorithm proposed in Ref. [22]. That is, we optimize the unit vectors site by site, and sweep the entire lattice until convergence is obtained. In order to improve the reliability of the optimizations, in this paper, for each set of physical parameters, 20 independent random initial conditions are adopted to carry out the optimization.

6. Global nonlocality and partial nonlocality

We will use two quantities to characterize the multipartite nonlocality in the models (Fig. 2). The first one is the *global nonlocality* measure $\mathcal{S}_g(|\psi\rangle)$, which is defined on a pure state $|\psi\rangle$ of the model [Fig. 2(a)]. Thereby, $\mathcal{S}_g(|\psi\rangle)$ measures multipartite nonlocality in the entire lattices. When necessary, we will use the logarithm measure (i.e., $\log_2 \mathcal{S}_g$) to display the numerical results. We mention that real materials often contain a large number of atoms (i.e., $L \to \infty$). Nevertheless,

[1] For an odd L, $|\psi_1\rangle$ would be the ground state and $|\psi_0\rangle$ would be the first-excited state.

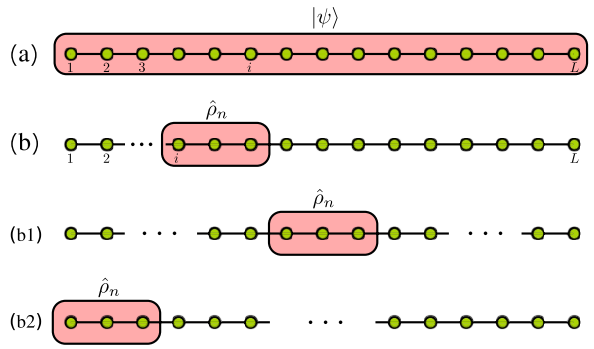

FIG. 2. Two quantities to characterize multipartite nonlocality in a 1D L-site lattice, i.e., (a) *global* nonlocality for a pure state $|\psi\rangle$ of the whole lattice, and (b) *partial* nonlocality for the reduced density matrices $\hat{\rho}_n$ of continuous n-site subchains. Green dots denote the lattice, and the pink rectangles denote the regions of interest. Two typical choices of the subchains are also illustrated, i.e., subchains locating at (b1) the middle part and (b2) the end of the lattice.

due to the limitations of experimental conditions, the actual measurement may only occur in a certain part of the system, rather than the entire lattice. Thereby, we will also analyze the *partial nonlocality* measure $\mathcal{S}_n(\hat{\rho}_n)$, which is defined on the reduced density matrices $\hat{\rho}_n$ of some concerned subchains [Fig. 2(b)]. Thereby, $\mathcal{S}_n(\hat{\rho}_n)$ measures multipartite nonlocality in the n-site subchains. Moreover, in this paper, two typical subchains are involved, that is, subchains at the middle part [Fig. 2(b1)] and at the end [Fig. 2(b2)] of the lattice.

IV. UNIFORM MODEL

A. Global nonlocality

We will analyze the global nonlocality in the uniform model in Eq. (6) from three aspects. First, we will offer an overall description about the influence of the chemical potential upon the global nonlocality in the model. Second, we will pay attention to the critical point at $U_{0c} = 2$ and use the nonlocality measure to characterize the QPT. Third, we will carry out a scaling analysis on our finite-L results and figure out the large-L limit.

The global nonlocality measure as a function of the chemical potential U_0 for the uniform model is shown in Fig. 3(a). These curves would also be the starting point for all the following discussions. First of all, for any fixed L, as U_0 increases, $\log_2 \mathcal{S}_g$ decreases monotonically. For both $|\psi_0\rangle$ and $|\psi_1\rangle$, we numerically find that when $U_0 = 0$ we have $\mathcal{S}_g = 2^{\frac{L-1}{2}}$, which is the maximal value allowed by quantum mechanics. Thereby, the highest rank inequality $\mathcal{S}_n \leqslant 2^{\frac{L-2}{2}}$ is violated and genuine multipartite nonlocality is observed. On the other hand, in the large-U_0 regions, $\log_2 \mathcal{S}_g$ is quite small. For $|\psi_0\rangle$, we expect $\log_2 \mathcal{S}_g$ would tend to be zero with $U_0 \to \infty$, since the ground state tends to be $|1, 1, 1, \ldots, 1\rangle$. For $|\psi_1\rangle$, which has an odd parity, when U_0 is rather large but still finite, it becomes a superposition state of the states $|0, 1, 1, \ldots, 1\rangle$, $|1, 0, 1, \ldots, 1\rangle$, $|1, 1, 0, \ldots, 1\rangle$, and so on. We have numerically checked $|\psi_1\rangle$ for $U_0 = 1000$, and found that the lowest rank Bell-type inequality $\mathcal{S} \leqslant 2^0$ is violated, but other inequalities are never violated for $L = 2, 4, \ldots, 12$.

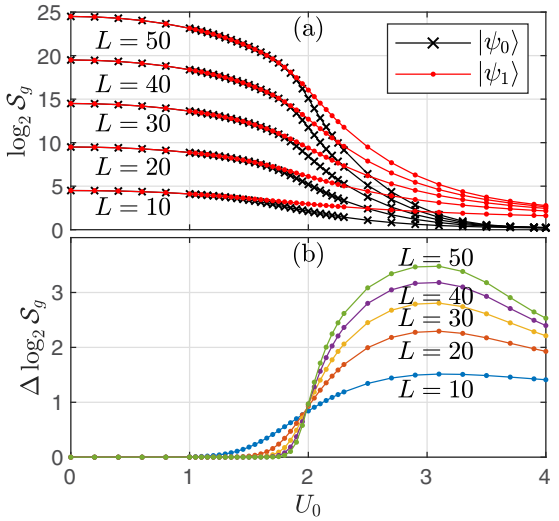

FIG. 3. (a) Global nonlocality measure as a function of the chemical potential for the uniform model (i.e., $\mu_i = U_0$) with length $L = 10, 20, \ldots, 50$. $U_{0c} = 2$ is the topological QPT point for infinite-size lattices. The crosses and dots correspond to the ground states $|\psi_0\rangle$ and $|\psi_1\rangle$ in the $P = 0$ and $P = 1$ sectors, respectively. The curves reveal how the chemical potential gradually destroys the global nonlocality in finite-size lattices. (b) The difference between $\log_2 \mathcal{S}_g(|\psi_1\rangle)$ and $\log_2 \mathcal{S}_g(|\psi_0\rangle)$. In the large-$L$ limit, $\Delta \log_2 \mathcal{S}_g$ vanishes for $U_0 < U_{0c}$ and is rather large for $U_0 > U_{0c}$, and thus signals the critical point $U_{0c} = 2$.

Thereby, $|\psi_1\rangle_{U_0 \gg 1}$ would merely present rather low hierarchy of multipartite nonlocality with the current Bell-type inequalities. Finally, Fig. 3(a) offers an overall description that as the chemical potential U_0 increases, the model gradually changes from states with genuine multipartite nonlocality to states with relatively low hierarchy of multipartite nonlocality (for $|\psi_1\rangle$) or product states (for $|\psi_0\rangle$).

Then we pay our attention to the critical point $U_{0c} = 2$. In the large-L limit, $|\psi_1\rangle$ and $|\psi_0\rangle$ would become degenerate for $U_0 < 2$. Thus, it is well known that their energy difference ΔE can be used as an order parameter of the phase transition, i.e., $\Delta E = 0$ for $U_0 < 2$ and $\Delta E \neq 0$ for $U_0 > 2$. In Fig. 3(a), one can see that $\log_2 \mathcal{S}(|\psi_0\rangle)$ and $\log_2 \mathcal{S}(|\psi_1\rangle)$ are equal to each other in most regions of the topologically nontrivial phase $U_0 < 2$, and are significantly different from each other in the topologically trivial phase $U_0 > 2$. Thereby, we have calculated their difference, i.e.,

$$\Delta \log_2 \mathcal{S}_g = \log_2 \mathcal{S}_g(|\psi_1\rangle) - \log_2 \mathcal{S}_g(|\psi_0\rangle), \tag{16}$$

and the result is shown in Fig. 3(b). As L increases, $\Delta \log_2 \mathcal{S}_g$ vanishes rapidly for $U_0 < 2$, and increases steadily for $U_0 > 2$. Thereby, $\Delta \log_2 \mathcal{S}_g$ offers an alternative perspective for us to characterize the difference between $|\psi_0\rangle$ and $|\psi_1\rangle$, and consequently, detect this topological QPT.

Furthermore, in Fig. 3(a) one may find that as U_0 increases, the nonlocality measure changes slowly in noncritical regions and changes quickly in the vicinity of $U_{0c} = 2$. Therefore, we have calculated the first-order derivative of the measures and the results are present in Fig. 4. We find that $\frac{\partial \log_2 \mathcal{S}_g}{\partial U_0}$ shows a peak in the vicinity of $U_{0c} = 2$ even L is quite small, i.e., $L = 20$. Moreover, as L increases, the peak value increases

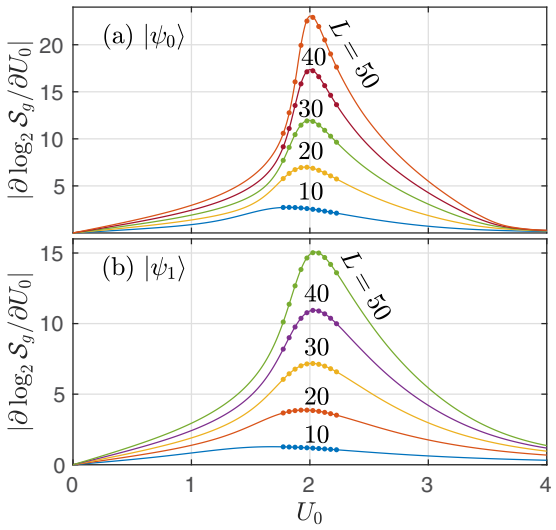

FIG. 4. The first-order derivative of the global nonlocality measure with respect to the chemical potential U_0 in the uniform model for (a) $|\psi_0\rangle$ and (b) $|\psi_1\rangle$. The derivative shows a peak in the vicinity of the critical point $U_{0c} = 2$. As L increases, the peak increases steadily and the FWHM gradually narrows. It indicates that in the large-L limit multipartite quantum correlations in the model change dramatically at the critical point.

steadily and the full width at half maxima (FWHM) gradually narrows.[2] In particular, for the ground state $|\psi_0\rangle$, when L is large enough, the peak is quite close to the critical point $U_{0c} = 2$ for $L \geqslant 30$. Thereby, in the large-L limit, it is expected that a sharp peak (in other words, a dramatic change in $\log_2 \mathcal{S}(|\psi_0\rangle)$) would be observed at $U_{0c} = 2$. We conclude that the topological QPT is accompanied by a dramatic change of multipartite quantum correlations in the model.

We have already involved some qualitative discussion about the large-L limit. Now we begin a quantitative analysis. In previous papers about 1D translation-invariant models, it has been found that in the large-L limit, the nonlocality measure $\mathcal{S}$ scales as [22]

$$\log_2 \mathcal{S} \sim \mathcal{K}L + b, \tag{17}$$

with $\mathcal{K}$ and b two fitting parameters. It is clear that the slope $\mathcal{K}$ plays a central role in characterizing the large-L behavior. In fact, $\mathcal{K}$ has a clear physical meaning. Let us reconsider Eq. (3), i.e.,

$$\log_2 \mathcal{S} \leqslant \frac{L - g}{2}. \tag{18}$$

For the highest hierarchy of multipartite nonlocality, one has $g \ll L$ and consequently, $\log_2 \mathcal{S} \sim \frac{L}{2}$. In other words, we have $\mathcal{K} = \frac{1}{2}$. For the lowest hierarchy of multipartite nonlocality, we have $g \sim L$, and consequently, $\mathcal{K} \to 0$. Thereby, the quantity $\mathcal{K}$ offers an overall description of multipartite nonlocality in the large-L limit.

[2]FWHM characterizes the sharpness of a peak. We use U_ℓ and U_r to denote the two potentials which satisfy $f(U_0) = \frac{1}{2} \max_{U_0} f(U_0)$ with $f(U_0)$ denoting the curves in Fig. 4. Then the quantity $\Delta U_0 = |U_r - U_\ell|$ is just the FWHM. As L increases, ΔU_0 decreases gradually.

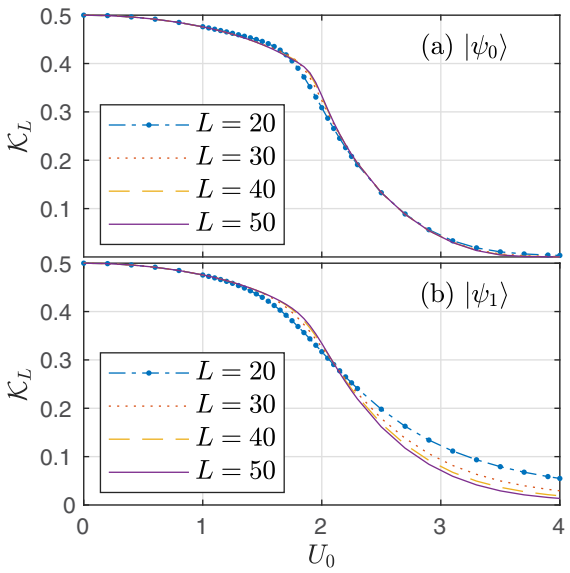

FIG. 5. Data collapse of the global nonlocality measure in the finite-size uniform model, where $\mathcal{K}_L$ is defined in Eq. (19). The quantity $\mathcal{K} = \lim_{L\to\infty} \mathcal{K}_L$ with $\mathcal{K} \in [0, \frac{1}{2}]$ is a measure of the overall multipartite nonlocality in infinite-size lattices.

We try to extract the value of $\mathcal{K}$ from our finite-L results. Considering Eq. (17), we define the finite-size slope $\mathcal{K}_L$ as

$$\mathcal{K}_L = \frac{\log_2 \mathcal{S}(L) - \log_2 \mathcal{S}(L - \Delta L)}{\Delta L}, \tag{19}$$

with some fixed ΔL. It is expected that $\mathcal{K}_L$ would converge in the large-L limit,

$$\mathcal{K} = \lim_{L\to\infty} \mathcal{K}_L. \tag{20}$$

The finite-size slope $\mathcal{K}_L$ with different L is illustrated in Fig. 5. First of all, when L is large enough, the $\mathcal{K}_L(U_0)$ curves with various L tend to overlap each other, which can be regarded as a signal of convergence for the large-L limit. Moreover, when $U_0 = 0$, we have $\mathcal{K} = 0.5$, i.e., the ground state presents genuine multipartite nonlocality. When U_0 is rather large, $\mathcal{K}$ is quite small (or even zero), which indicates low hierarchy of multipartite nonlocality (or product states). One can see that Fig. 5 offers us an intuitive and overall description about multipartite nonlocality in the infinite-size model.

B. Partial nonlocality

We turn our attention to partial nonlocality. The analytical results of the nonlocality measure $\mathcal{S}_2$ in infinite-size models are shown in Fig. 6. Its derivative presents a clear divergence at the critical point $U_{0c} = 2$. Nevertheless, for any U_0 one can see that the lowest rank of Bell inequality $\mathcal{S}_n \leqslant 1$ is not violated. In other words, quantum nonlocality is not observed. Therefore, it is necessary to consider large n.

For such a purpose, we will study finite-size models with total length $L = 200$, and the lengths of the concerned subchains are $n = 2, 4, 6, \ldots, 12$. The setting $n \ll L$ is to help us capture the basic behavior of subchains in infinite-size lattices. For finite-size models, a brief description about the position

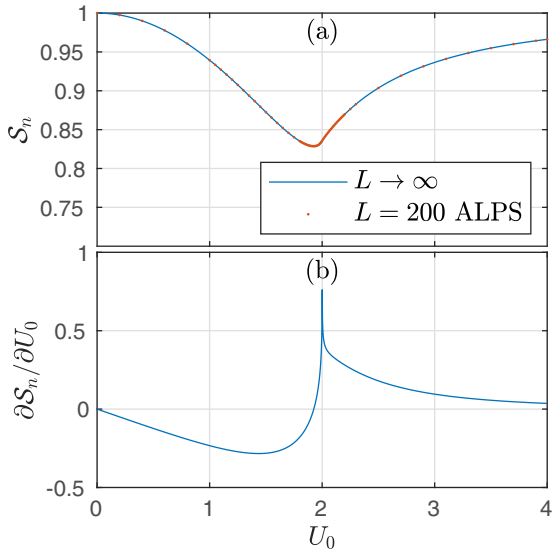

FIG. 6. Analytical results of (a) partial nonlocality measure and (b) its derivative in the infinite-size uniform model with $n = 2$. $U_{0c} = 2$ is the critical point. Numerical results from ALPS are shown for a comparison purpose.

dependence of the partial nonlocality would be helpful. Please see Fig. 7. In the middle part of the lattice, $\mathcal{S}_n$ shows no dependence upon i, i.e., it is translation invariant. In the boundary area, $\mathcal{S}_n$ presents some dependence upon i. Furthermore, when the system is far away from the critical point $U_{0c} = 2$ (i.e., $U_0 = 1.0$ and $U_0 = 2.9$), the boundary area is quite narrow. Nevertheless, when the system is near the critical point (i.e., $U_0 = 1.9$), one can see the boundary area is rather wide. In the following discussions, we will just consider two typical subchains, that is, the subchain at the midpoint of the lattice and the subchain at the left end of the lattice.

In Fig. 8(a), we present the partial nonlocality for subchains at the midpoint of the lattice. We will use the nonlocality measure $\mathcal{S}_n$ to characterize the two quantum phases, and then pay our attention to the critical point $U_{0c} = 2$.

First, in most regions of the topologically nontrivial phase in $U_0 < 2$, as n increases, $\mathcal{S}_n$ decreases gradually. As a result, the lowest rank Bell inequality $\mathcal{S}_n \leqslant 1$ is not violated. Therefore, no quantum nonlocality can be observed by testing the

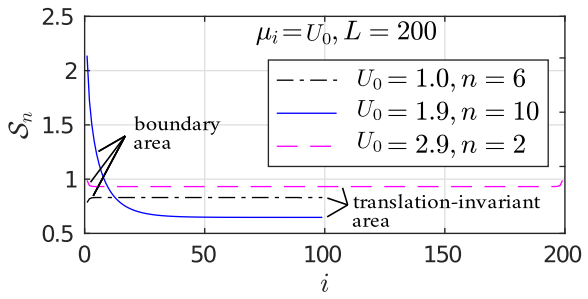

FIG. 7. Position dependence of the partial nonlocality $\mathcal{S}_n$ in the uniform model. i and n are the location and the length of the subchain, respectively. In a wide area in the middle of the lattice, $\mathcal{S}_n$ is translation invariant. Strong boundary effect is observed when $U_0 \approx U_{0c} = 2$.

current Bell-type inequalities on the subchains. Second, for the quantum phase in $U_0 > 2$, when $n \geqslant 6$, we find $\mathcal{S}_n \leqslant 1$ is violated, and thus quantum nonlocality is observed. Furthermore, as n increases, $\mathcal{S}_n$ is enhanced. In particular, for $2 < U_0 < 3$, $\mathcal{S}_n$ increases significantly as n increases. Therefore, the quantum phase in $U_0 > 2$ is featured with the presence of nontrivial multipartite quantum nonlocality in the subchains. Third, we consider the critical point $U_{0c} = 2$. When n is large enough, one can see that the first-order derivative $\frac{\partial \mathcal{S}_n}{\partial U_0}$ would tend to diverge in the vicinity of $U_{0c} = 2$. It indicates that the QPT is accompanied by fundamental changes of multipartite quantum correlations in these subchains.

In Fig. 8(b), we present the partial nonlocality for subchains at the end of the lattice. First of all, on the two sides of the critical point, the behavior of $\mathcal{S}_n(U_0)$ is qualitatively different. Moreover, $\mathcal{S}_n$ shows a peak in the vicinity of $U_{0c} = 2$. Thereby, the result is quite similar to Fig. 8(a). Nevertheless, there is a subtle difference; that is, in the vicinity of $U_{0c} = 2$ of Fig. 8(b), $\frac{\partial \mathcal{S}_n}{\partial U_0}$ does not present a strong signal of divergence. We would like to mention that a QPT is a quantum many-body phenomenon. For translation-invariant lattices, subchains in the middle part of the lattices are more representative than the edge subchains to capture the bulk property of the models. That is why the former presents a sharper signal of the QPT than the latter.

It may be interesting to carry out a scaling analysis of the partial nonlocality in the model. Let us consider the peak of the $\mathcal{S}_n(U_0)$ curves, i.e.,

$$\mathcal{S}_n^* = \max_{U_0} \mathcal{S}_n(U_0). \tag{21}$$

In Fig. 8(c), we have illustrated the dependence of $\log_2 \mathcal{S}_n^*$ upon n. It is clear that when n is large enough, $\log_2 \mathcal{S}_n^*$ also scales linearly; i.e.,

$$\log_2 \mathcal{S}_n^* \sim \mathcal{K}' n + b'. \tag{22}$$

In our settings, we have $n \ll L$. Thereby, we expect this scaling should hold for long subchains in infinite-size lattices.

V. INCOMMENSURATE MODELS

In this section, we will investigate the incommensurate model defined in Eq. (7). We mention that the Z_2 symmetry survives, and thereby we have also considered both $|\psi_0\rangle$ and $|\psi_1\rangle$ in our calculations. However, we numerically find that in this incommensurate model, the global nonlocality of the two states are approximately equal to each other for any μ. A possible reason is that these incommensurate potentials have weakened (or eliminated) the difference between the lowest lying state with an odd particle number and the lowest lying state with an even particle number. Thereby, in our following discussions, we just report our results for $|\psi_0\rangle$.

One of the key features of the incommensurate model is that the translation invariance is broken. Thereby, first of all, we will use the position dependence of the partial nonlocality to offer an intuitive description of the model. Please see Fig. 9. One sees that $\mathcal{S}_n$ exhibits some *irregular periodicity*. It results from the cosine function in the incommensurate potentials, i.e., $\mu_i = \mu \cos(2\pi i\alpha)$. Specifically, strong irregularity is observed in the vicinity of critical point $\mu_c = 4$.

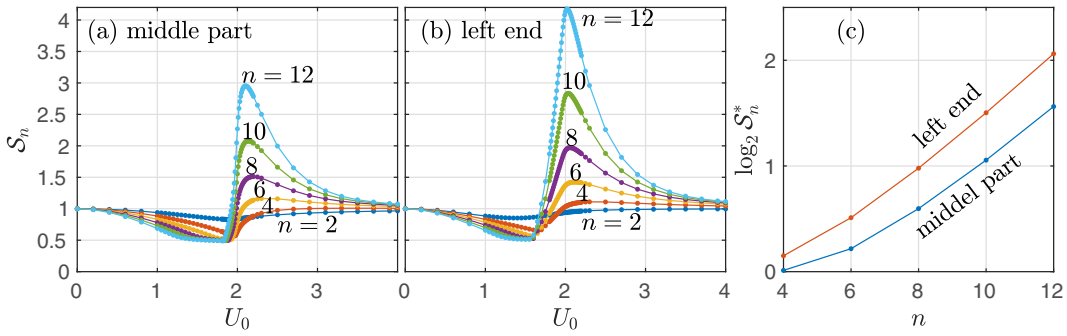

FIG. 8. Partial nonlocality measure for n-site subchains at (a) the middle part and (b) the left end of the uniform model. The total length of the model is $L = 200$ and n denotes the length of the subchains. For panel (a), in most regions of the topologically nontrivial phase $U_0 < 2$, the Bell inequality $\mathcal{S}_n \leqslant 1$ is not violated, and thus quantum nonlocality is not observed. In the quantum phase $U_0 > 2$, multipartite quantum nonlocality is observed. When n is large enough, $\mathcal{S}_n$ tends to be singular at the critical point $U_{0c} = 2$. For panel (b), the measure just presents a peak in the vicinity of $U_{0c} = 2$. (c) Scaling analysis of the peak value of the partial nonlocality measure, i.e., $\mathcal{S}_n^* = \max_{U_0} \mathcal{S}_n(U_0)$. $\log_2 \mathcal{S}_n^*$ scales linearly when n is large enough.

Next, we shall resort to the global nonlocality and the partial nonlocality to characterize the ground state $|\psi_0\rangle$ and the QPT in the model.

A. Global nonlocality

The global nonlocality in the incommensurate model is illustrated in Fig. 10(a). In the limit $\mu \to 0$, the models would be reduced into the uniform model. Thus, genuine multipartite nonlocality survives and we still have $\mathcal{S}_g|_{\mu=0} = 2^{\frac{L-1}{2}}$, or alternatively,

$$\log_2 \mathcal{S}_g|_{\mu=0} = \frac{L-1}{2}. \tag{23}$$

As μ increases, the measure decreases gradually. One can see that the trend of the $\log_2 \mathcal{S}_g(\mu)$ curves is quite similar to that in the uniform mode.

We pay attention to the L dependence of the nonlocality measure $\mathcal{S}_g$. Unlike the uniform model, it seems that when the incommensurate potential strength μ is large enough, the scaling formula $\log_2 \mathcal{S}_g \sim \mathcal{K}L + b$ does not hold for short chains. For instance, let us consider $\mu_c = 4$ in Fig. 10(a), where as L increases, $\log_2 \mathcal{S}_g$ does not increase linearly. Therefore, in order to capture the large-L behavior, the finite-L slope $\mathcal{K}_L$ used in the uniform model may not be the best quantity to be considered. Instead, we try to rescale the $\log_2 \mathcal{S}_g(\mu)$ curves as

$$\log_2 \tilde{\mathcal{S}}_g(\mu) = \frac{1}{\frac{L-1}{2}} \log_2 \mathcal{S}_g(\mu), \tag{24}$$

where the scale factor is related to $\mathcal{S} = 2^{\frac{L-1}{2}}$, i.e., the maximal value of the nonlocality measure allowed by quantum mechanics. The results are illustrated in Fig. 10(b). It is quite clear that the rescaled curves for $L = 40$, 50, and 60 almost overlap each other. It indicates that for any given μ, in the large-L limit we have

$$\lim_{L\to\infty} \log_2 \tilde{\mathcal{S}}_g = \lim_{L\to\infty} \frac{1}{\frac{L-1}{2}} \log_2 \mathcal{S}_g \to \text{const.} \tag{25}$$

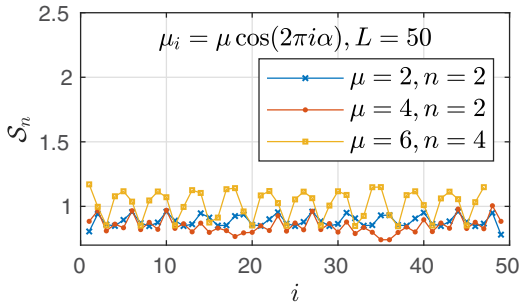

FIG. 9. Position dependence of the partial nonlocality $\mathcal{S}_n$ in the incommensurate model. i and n are the location and the length of the subchain, respectively. $\mathcal{S}_n$ exhibits some irregular periodicity for any μ. Rather strong irregularity is observed in the vicinity of the critical point $\mu_c = 4$.

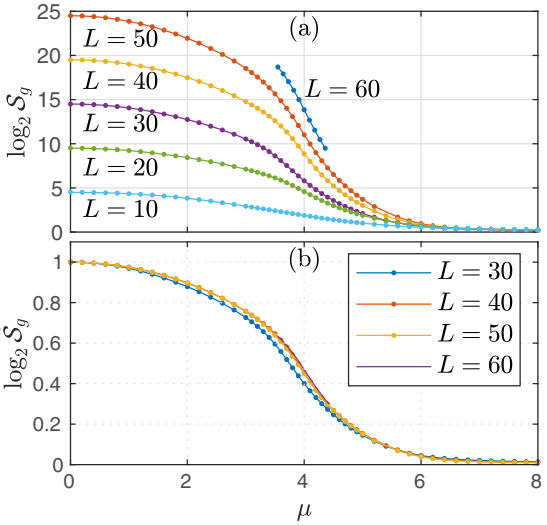

FIG. 10. (a) Global nonlocality measure $\log_2 \mathcal{S}_g$ and (b) the rescaled measure $\log_2 \tilde{\mathcal{S}}_g = (\log_2 \mathcal{S}_g)/\frac{L-1}{2}$ as a function of the chemical potential strength μ in the incommensurate model [i.e., $\mu_i = \mu \cos(2\pi i\alpha)$]. The collapse of the $\log_2 \tilde{\mathcal{S}}_g(\mu)$ curves indicates that multipartite correlations in the infinite-size incommensurate model can be characterized quite well by global nonlocality.

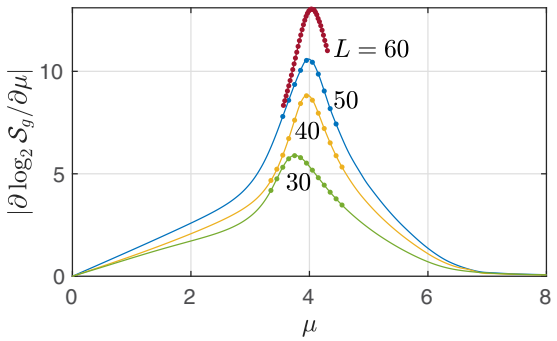

FIG. 11. The first-order derivative of the global nonlocality measure as a function of the chemical potential strength μ in the incommensurate model. The derivative shows a peak in the vicinity of the critical point $\mu_c = 4$. As L increases, the peak increases steadily. It indicates that the quantum phase transition can be characterized by a dramatic change of multipartite nonlocality in the ground state.

In other words, in this incommensurate model the scaling behavior

$$\log_2 \mathcal{S}_g \sim \mathcal{K}L + b \tag{26}$$

should recover in the large-L limit.

We mention that in Fig. 10(b), $\log_2 \tilde{\mathcal{S}}_g = 1$ indicates genuine multipartite nonlocality, and $\log_2 \tilde{\mathcal{S}}_g = 0$ indicates that no nonlocality could be observed by the current Bell-type inequalities. Thereby, Fig. 10(b) captures the process how the incommensurate potentials destroy multipartite nonlocality in infinite-size models.

We then turn our attention to the critical point $\mu_c = 4$. In Fig. 11, we have illustrated the first-order derivative of the nonlocality measure. One can see that for finite L, the derivative shows a peak in the vicinity of $\mu_c = 4$. Moreover, as L increases, the peak value increases steadily. Thereby, just as in the uniform model, the QPT in the incommensurate model is also accompanied by dramatic changes of multipartite nonlocality in the ground state. We would like to mention that this QPT has been characterized with the average two-site correlation function $\bar{C} = \frac{1}{L}\sum_i C_{i,i+\frac{L}{2}}$ in the model with periodic boundary conditions [38]. In particular, it is found unambiguously that $\bar{C}$ is nonzero in $\mu_c < 4$ and vanishes in $\mu > 4$, and thus $\bar{C}$ signals the QPT perfectly. One might find that the definition of $\bar{C}$ is not very intuitive. Nevertheless, a possible reason for its success is that $\bar{C}$ characterizes some quantum correlations spreading among multisites (rather than just two sites) in the lattice. In this paper, our results about $\mathcal{S}_g$ in Figs. 10 and 11 show that multipartite correlations offer another informative (and much more intuitive) perspective to characterize the ground state and the QPT in this model.

B. Partial nonlocality

In this section, we investigate the partial nonlocality in the incommensurate model. Considering its incommensurability, we may need to analyze long chains. Thereby, we have set $L = 500$ in our simulations. We have also considered the two typical subchains in Fig. 2, and the final results are shown in Fig. 12. First of all, most of the results are similar to those in the uniform model. For instance, in Fig. 12(a), in the vicinity of the critical point $\mu_c = 4$, the nonlocality measure for the middle subchains presents a singularity. Moreover, in most regions of $\mu < \mu_c$, the lowest rank of Bell-type inequalities $\mathcal{S} \leqslant 1$ is not violated.

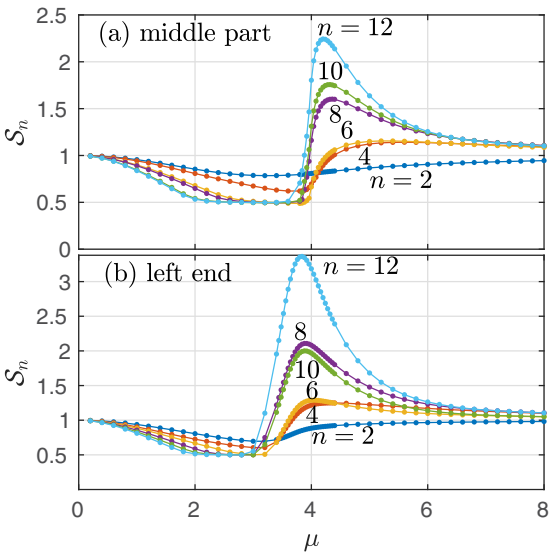

FIG. 12. Partial nonlocality measure for n-site subchains at (a) the middle part and (b) the left end of the incommensurate model. The total length of the model is $L = 500$ and n denotes the length of the subchains. The behavior of $\mathcal{S}_n$ is quite similar to that in the uniform model. A key difference is that the linear scaling behavior observed in the uniform lattice in Fig. 8(c) no longer holds in the incommensurate lattice.

However, as n increases, one sees that the peak value of the $\mathcal{S}_n(\mu)$ curves does not present a clear scaling behavior. Especially, in Fig. 12(b), as n increases, the measure $\mathcal{S}_n$ for the left end subchains even does not present a monotonous increment. For instance, at $\mu_c = 4$ we have $\mathcal{S}_{12} > \mathcal{S}_8 > \mathcal{S}_{10}$. The n dependence of the partial nonlocality measure in this model is quite different from that in the uniform model [see Fig. 8(c)] and reflects the incommensurate nature of the model.

A comment on Fig. 12(a) is necessary. It is quite clear that the first-order derivative $\frac{\partial \mathcal{S}_n}{\partial \mu}$ tends to be infinite in the large-n limit, which is a strong signal for the QPT. It is interesting that partial nonlocality of subchains can signal the QPT in an incommensurate model. The underlying mechanics is as follows. When incommensurate potentials are present, although translation invariance is destroyed, the ground state still presents some irregular periodicity along the lattice, as disclosed by the position dependence of the partial nonlocality in Fig. 9. When the subchain length is significantly greater than the space period of the wave functions, the partial nonlocality can capture part of the bulk properties (such as the QPT) of the model. That is why the partial nonlocality measure for the middle subchains can present a clear signal for the QPT at $\mu_c = 4$.

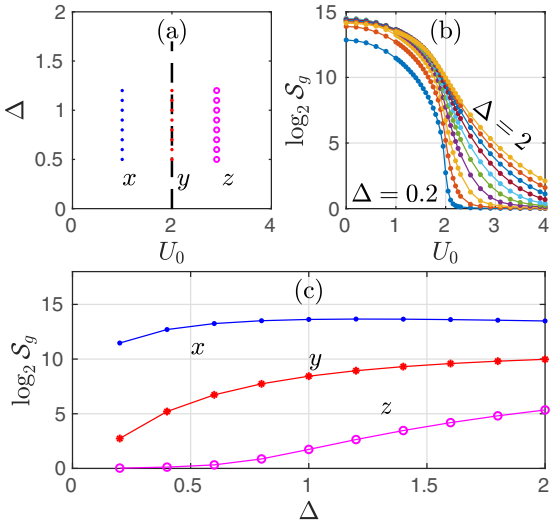

FIG. 13. (a) Phase diagram of the uniform model (i.e., $\mu_i = U_0$) on the Δ-U_0 plane, with $U_{0c} = 2$ being the phase boundary. x and z denote two paths in parallel with the phase boundary. (b) Global nonlocality measure with $\Delta = 0.2, 0.4, 0.6, \ldots, 2.0$. The total length of the model is $L = 30$. In the vicinity of $U_{0c} = 2$, the derivative of $\log_2 \mathcal{S}_g$ always shows a maximum. (c) In the large-Δ region, when the system moves along the phase boundary, the nonlocality measure changes little in the SC phase (see path x), and changes considerably in the localized phase (see path z).

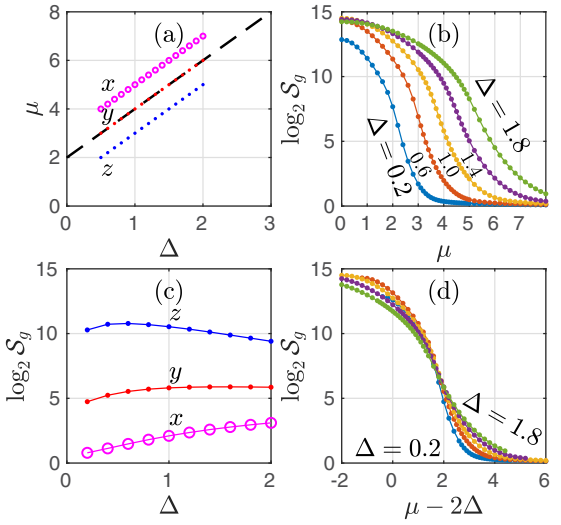

FIG. 14. (a) Phase diagram of the incommensurate model [i.e., $\mu_i = \mu \cos(2\pi i\alpha)$] on the μ-Δ plane, with the dashed line $\mu = 2\Delta + 2$ denoting the phase boundary. x and z denote two paths in parallel with the phase boundary. (b) Global nonlocality measure with various Δ. The total length of the model is $L = 30$. (c) In the large-Δ region, when the system moves along the phase boundary, the nonlocality measure decreases in the SC phase(see path z) and increases in the localized phase(see path x). (d) The nonlocality measure as a function of $\mu - 2\Delta$.

VI. INTERPLAY BETWEEN P-WAVE PAIRING INTERACTION Δ AND CHEMICAL POTENTIALS

In this section, we will use multipartite nonlocality to investigate the interplay between p-wave pairing interaction Δ and chemical potentials.

A. Uniform model

For the uniform model with any finite nonzero Δ, the critical point is still at $U_{0c} = 2$ [37]. The phase diagram is shown in Fig. 13(a). For several fixed Δ, we change U_0 gradually so as to cross the phase boundary, and the numerical results are shown in Fig. 13(b). One can see that the derivative of the nonlocality measure always presents a maximum in the vicinity of the critical point $U_{0c} = 2$. According to the finite-size analysis in Secs. IV and V, these maximum points correspond to sharp peaks when L is large enough. Therefore, we expect that in the large-L limit, the topological QPTs in the uniform models with finite Δ are accompanied by dramatic changes of multipartite nonlocality.

We then pay our attention to the influence of Δ upon the nonlocality curves. When Δ is small (i.e., $\Delta = 0.2$), the $\log_2 \mathcal{S}_g \sim U_0$ curve exhibits a sharp change around $U_{0c} = 2$. As Δ increases, the changing trend of the $\log_2 \mathcal{S}_g \sim U_0$ curves becomes flatter gradually. Furthermore, when Δ is large enough, we find the curves almost overlap each other in the SC phase ($U_0 < 2$), and do not overlap in the localized phase ($U_0 > 2$). This behavior is shown quantitatively in Fig. 13(c), where x and z correspond to the paths with $U_0 = 1$ (in the SC phase) and $U_0 = 2.9$ (in the localized phase), respectively. One sees that on the two sides of the phase boundary, when we tune the system along paths in parallel with the phase boundary, the nonlocality measure behaves quite differently.

B. Incommensurate model

In the incommensurate model [38], for any finite Δ, the critical points locate along the path $\mu_c = 2\Delta + 2$ in the phase diagram [see Fig. 14(a)]. For several fixed Δ, we change μ gradually so as to cross the phase boundary, and the corresponding numerical results are shown in Fig. 14(b). Again, we find $\frac{\partial \log_2 \mathcal{S}_g}{\partial \mu}$ always presents a maximum in the vicinity of the critical point $\mu_c = 2\Delta + 2$. We expect that in the large-L limit, the topological QPTs in the models would be accompanied by dramatic changes of multipartite nonlocality.

Next, just as in the uniform model in Fig. 13, we try to move the incommensurate model along paths which are in parallel with the phase boundary $\mu_c - 2\Delta = 2$. Let us consider three paths x (i.e., $\mu - 2\Delta = 2 + \delta$) and z (i.e., $\mu - 2\Delta = 2 - \delta$) with $\delta = 1$, which are illustrated in Fig. 14(a). The corresponding results about nonlocality are shown in Fig. 14(c). For path x in the localized phase, as Δ increases the nonlocality measure *increases* gradually. For path z in the SC phase, when Δ is not too small, as Δ increases the nonlocality measure *decreases* gradually. Thereby, along the two paths, the measure behaves in opposite ways. Nevertheless, this behavior is not specific just to these two paths with $\delta = 1$. In fact, in Fig. 14(d) we have redrawn the nonlocality curves as a function of $\mu - 2\Delta$, with $\Delta = 0.2, 0.6, 1.0, 1.4, 1.8$. By drawing vertical lines in Fig. 14(d), one can see clearly that the above opposite trends are general on the two sides of the phase boundary $\mu - 2\Delta = 2$.

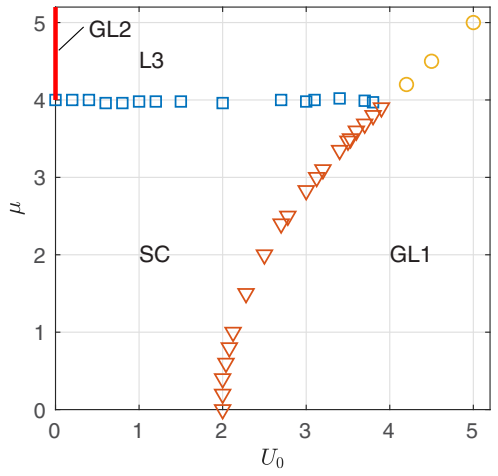

FIG. 15. Phase diagram of the mixed-potential model [i.e., $\mu_i = U_0 + \mu\cos(2\pi i\alpha)$] on the μ-U_0 plane. The ground states of the model have a topologically SC phase and three localized regions marked as GL1, GL2, and L3. The phase boundaries are obtained by analyzing the exact energy spectrum of the model with $L = 2000$.

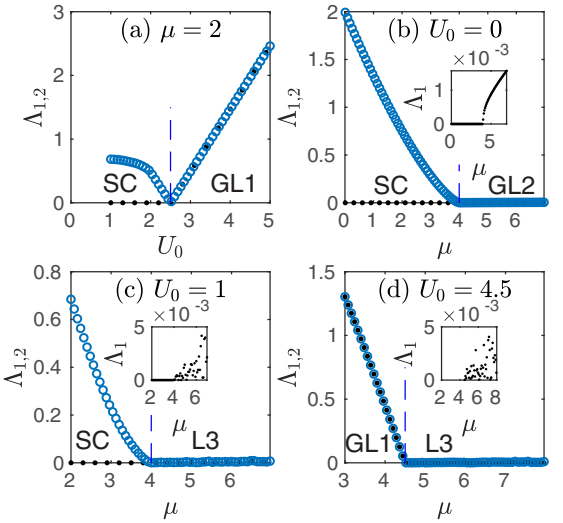

FIG. 16. The lowest two modes Λ_1 and Λ_2 in the energy spectrum of the mixed-potential model with the ground states crossing the phase boundaries. The length of the model is $L = 2000$.

Therefore, in both the uniform model and the incommensurate model, it is quite interesting that when the model moves in parallel with the phase boundary on the $\mu_i - \Delta$ plane, the ground-state nonlocality behaves quite differently on the two sides of the phase boundary. This result provides an alternative perspective to describe the phase transitions.

VII. INTERPLAY BETWEEN UNIFORM POTENTIALS U_0 AND INCOMMENSURATE POTENTIALS μ

In this section, we will consider the mixed-potential model with $\mu_i = U_0 + \mu\cos(2\pi i\alpha)$, and investigate the interplay between the uniform potential U_0 and the incommensurate potential μ. For simplicity, we shall fix $\Delta = 1$, and analyze the ground states on the $\mu - U_0$ plane.

A. Phase diagram and energy spectrum

First of all, the phase diagram of this mixed-potential model is unknown. Therefore, we have analyzed the exact energy spectrum Λ_n of the model with $L = 2000$ so as to figure out the phase diagram. Please see Fig. 15. There are four phases on the μ-U_0 plane, that is, an SC phase and three localized regions marked as GL1, GL2, and L3. The energy spectrum in these phases and in the corresponding phase transitions have been illustrated in Fig. 16.

When both U_0 and μ are weak (i.e., lower left corner on the phase diagram), the system would be in the SC phase. The SC phase is featured with an unambiguous zero-energy mode and a finite gap above zero energy [see Figs. 16(a)–16(c)]. When the uniform potential U_0 or the incommensurate potential μ is large enough, the SC phase would be destroyed, and the system would be driven into localized phases.

In situations where the incommensurate potential μ is weak and the uniform potential U_0 dominates (i.e., lower right corner on the phase diagram), the system would undergo a phase transition from the SC phase into the GL1 phase. In Fig. 16(a), we have shown the energy spectrum in an SC-GL1 transition by fixing $\mu = 2$ and changing U_0. The critical point locates at $U_{0c} = 2.5$. One can see that the GL1 phase does not have zero-energy mode. Instead, it is featured with an unambiguous energy gap. Moreover, it is clear that the topological QPT in the uniform model studied in Sec. IV is just an instance of the SC-GL1 transitions with $\mu = 0$.

When the uniform potential is absent and the incommensurate potential is strong (i.e., the μ axis in the phase diagram), the system would undergo a transition from the SC phase into the GL2 phase, which is just the topological QPT studied in the incommensurate model in Sec. V. In Fig. 16(b), we have shown the energy spectrum in the SC-GL2 transition, where the critical point locates at $\mu_c = 4$. From the inset of Fig. 16(b), one can see that the GL2 phase does not have zero-energy mode and has a nonzero gap. The gap increases as μ. Nevertheless, even with $\mu = 10$, we merely have $\Lambda_1 = 2.5 \times 10^{-3}$. Therefore, when μ is finite, the gap of the GL2 phase is rather narrow. Consequently, this phase just exists in a rather narrow region in the vicinity of the μ axis. A small uniform potential U_0 can easily destroy this phase and drive the system into other localized states in the L3 region.

In Fig. 16(c), we have presented the energy spectrum in an SC-L3 transition by fixing $U_0 = 1$ and changing μ. The system is in the L3 region for $\mu > 4$. From the inset of the figure one, can see that the L3 region is featured with a strong random fluctuation in Λ_1. We mention that for general U_0, the phase boundary between the SC phase and the L3 region is still located at $\mu_c = 4$. Please see the squares in Fig. 15. A rather slight offset from $\mu_c = 4$ should origin from the combination of the irrational number α in the incommensurate potential and finite-size effects in the one-dimensional lattices.

We have also considered a transition from the GL1 phase to the L3 region; please see Fig. 16(d). As shown in its inset, the L3 region is indeed featured with strong random fluctuation in Λ_1. Moreover, numerical result indicates that the boundary

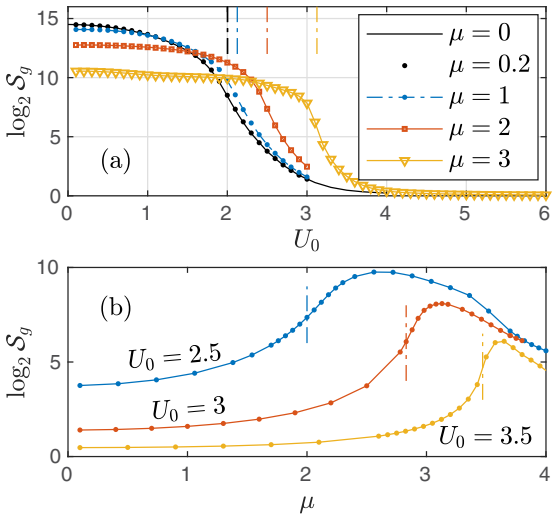

FIG. 17. Global nonlocality measure of the mixed-potential model as a function of (a) U_0 and (b) μ. The length of the model is $L = 30$. Vertical dashed lines denote the corresponding SC-GL1 critical points from Fig. 15. The derivative of the measure always presents a maximum in the vicinity of the critical points.

between the GL1 phase and the L3 region is just along the line $\mu = U_0$ on the phase diagram.

B. SC-GL1 transitions

We shall characterize the SC-GL1 transitions with multipartite nonlocality. We consider two approaches to cross the phase boundary, i.e., along the horizontal direction or the vertical direction on the phase diagram.

In the first approach, the numerical results of the $\log_2 \mathcal{S}_g \sim U_0$ curves with several fixed μ are shown in Fig. 17(a). For a comparison purpose, locations of the critical points from Fig. 15 have also been illustrated in the figure (see the dashed vertical lines). For each μ, one can find that the nonlocality measure always presents a maximum in the vicinity of the corresponding critical point and thus signals the QPT.

Then let us take a closer look at the results and regard the incommensurate potential μ as a perturbation to the uniform model. That is, we express the Hamiltonian of the mixed-potential model as

$$\hat{H} = \hat{H}_0 + \hat{H}', \tag{27}$$

where $\hat{H}_0$ describes the 1D spinless fermion quantum model with a uniform potential, given by Eqs. (4) and (6), and $\hat{H}'$ denotes the perturbation from the incommensurate chemical potentials,

$$\hat{H}' = -\mu \sum_{i=1}^{L} \cos(2\pi i\alpha) c_i^\dagger c_i. \tag{28}$$

The effect of the perturbation can be evaluated by the difference between the $\log_2 \mathcal{S}_g \sim U_0$ curve with $\mu = 0$ and that with a small μ. In Fig. 17(a), it is clear that the curves of $\mu = 0$ (the black solid line) and $\mu = 0.2$ (the black dots) almost overlap each other. It means that the topological QPT in the uniform model is quite robust under the perturbation. As shown in the phase diagram in Fig. 15, when μ is zero, the SC-GL1 transition point just locates at $U_{0c} = 2$. The incommensurate potential μ of course would have some effect upon the SC-GL1 critical point. Nevertheless, no considerable shift of the critical point from $U_{0c} = 2$ can be observed when $\mu \leqslant 0.6$. This robustness has two causes. First, both the SC phase and the GL1 phase have a large energy gap. Second, the cosine-function-modulated incommensurate potential may not be regarded as an efficient global perturbation. It is expected that a topological QPT would be robust against local perturbation [53].

We mention that a quite different situation emerges in the incommensurate model. For the pure incommensurate model (i.e., $U_0 = 0$), there is an SC-GL2 transition at $\mu_c = 4$. This transition is also a topological QPT. Nevertheless, as shown in the phase diagram of Fig. 15, a slightly nonzero U_0 would destroy the GL2 phase, and the system would be driven into the L3 region. Thus, this topological QPT turns out to be quite fragile. This frangibility also has two causes. First, as we have shown, the energy gap of the GL2 phase is rather narrow (i.e., $\Lambda_1 \approx 10^{-3}$). Second, the uniform potential U_0 is unambiguously a global (rather than local) perturbation.

Let us turn our attention back to the SC-GL1 boundary, and cross this boundary by fixing U_0 and changing μ. The numerical results are illustrated in Fig. 17(b). First, the dashed vertical lines denote the critical points from Fig. 15. One finds the nonlocality measure always presents a maximum in the vicinity of the critical point. Second, as μ increases, the $\log_2 \mathcal{S}_g \sim \mu$ curve behaves quite differently from the monotonically decreasing curves in the incommensurate model (i.e., with $U_0 = 0$) and the uniform model (i.e., $\mu = 0$). Instead, a round peak is observed in the SC phase. Thereby, the interplay between U_0 and u can induce rich changes in multipartite nonlocality in the mixed-potential models.

Figures 17(a) and 17(b) together indicate that the mixed-potential model presents high nonlocality in the SC phase and low nonlocality in the LG1 phase. Furthermore, when the system crosses the phase boundary, the nonlocality measure would always exhibit a maximum in its first-order derivative. According to the finite-size analysis in previous sections, it is expected that in the thermodynamic limit, the SC-GL1 transitions in the mixed-potential models would be accompanied by dramatic changes of multipartite correlations in the ground states.

C. L3 region

We have already analyzed the SC-GL2 phase transition in Sec. V and the SC-GL1 phase transitions in Sec. IV and VII B. On the phase diagram, the only region which has not yet been covered is the L3 region. In this section, we pay our attention to this region.

First, we try to enter the L3 region on the phase diagram by fixing U_0 and changing μ, and the results of nonlocality are shown in Fig. 18. One can see that while the nonlocality measure keeps analytic in all other phases, it exhibits a multi-kink-point structure in the L3 region. In order to investigate the origin of this multi-kink-point structure, we shall investigate a short chain with $L = 20$. We have considered the ground states in both the $P = 0$ sector and the $P = 1$

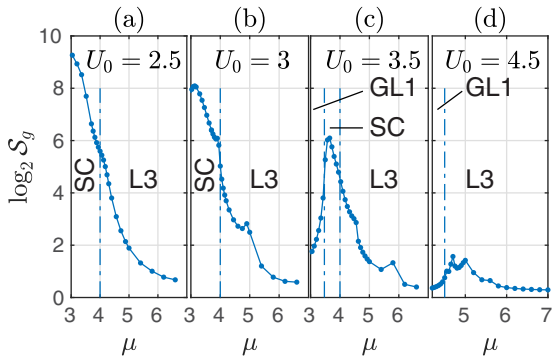

FIG. 18. Global nonlocality measure of the mixed-potential model as a function of μ for several U_0. The length of the model is $L = 30$. Vertical dashed lines denote the phase boundary from Fig. 15. The L3 region is featured with a multi-kink-point structure in the nonlocality curves.

section, and the results are shown in Fig. 19(a). Moreover, for a comparison purpose, the energy gap of the model has also been illustrated in Fig. 19(b). One can check that every kink point in the $\log_2 \mathcal{S}_g \sim \mu$ curves is related to a level crossing point (i.e., the turning points of Λ_1). We have also considered a model with $L = 200$ [Fig. 19(c)]. It is clear that as L increases, more level crossings would occur in the L3 region. Therefore, the randomness in the spectrum of Figs. 16(c) and 16(d) results from frequent level crossings. Consequently, the $\log_2 \mathcal{S}_g \sim \mu$ curve would exhibit a multi-kink-point structure for finite L and would present a randomness feature in the thermodynamic limit.

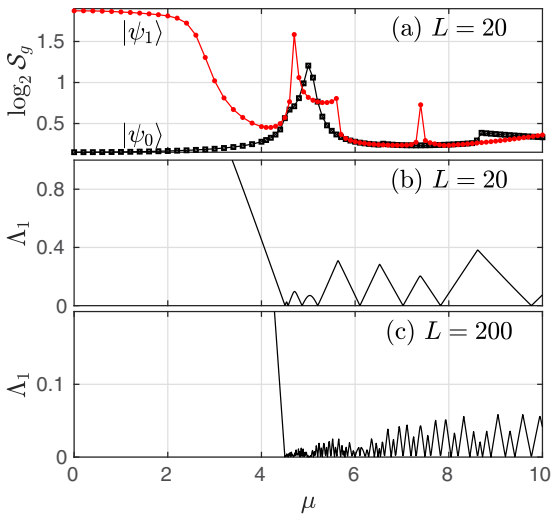

FIG. 19. Origin of the multi-kink-point structure in the L3 region by considering $U_0 = 4.5$. (a) Global nonlocality measure for the lowest lying states $|\psi_0\rangle$ and $|\psi_1\rangle$ in the $P = 0$ and $P = 1$ sectors, respectively. (b) Λ_1 in the spectrum of the model with $L = 20$. $\Lambda_1 = 0$ are related to level crossings between the two lowest lying states, and the sharp spikes of Λ_1 are related to level crossings in the excited states. There is a clear correspondence between the kink points in the nonlocality curve and the level crossings. (c) Λ_1 of the model with $L = 200$.

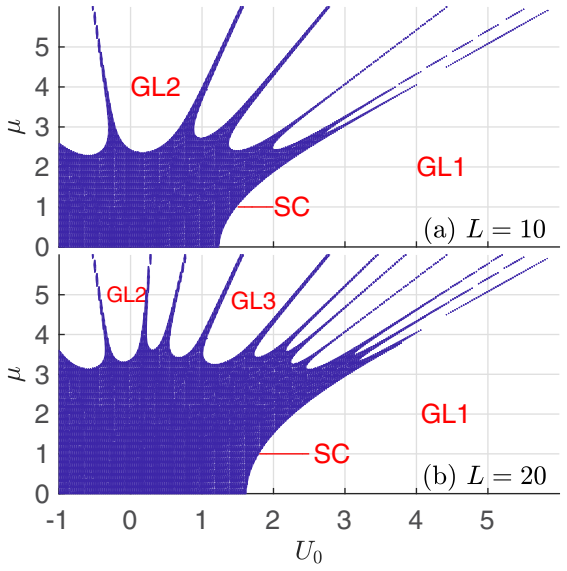

FIG. 20. Location of the zeros of Λ_1 (indicated by shaded area) of the mixed-potential model on the μ-U_0 plane with (a) $L = 10$ and (b) $L = 20$.

Since the key feature (that is, the randomness) of the region is caused by level crossings, this region may be better understood and described by considering level crossings for short chains in details and taking finite-size effects into account.

In Fig. 20, we have illustrated the location of the zeros of Λ_1 by the shaded area on the μ-U_0 plane. The results are numerically obtained by calculating the curved surface $\Lambda_1(\mu, U_0)$ and setting a rather small threshold ϵ as $\Lambda_1(\mu, U_0) \leqslant \epsilon$.

The wide shaded area in the lower left corner of Fig. 20 corresponds to the SC phase, which has unambiguous zero-energy mode (i.e., $\Lambda_1 = 0$). Nevertheless, shaded areas in other phases correspond to level crossings. For instance, in the $L = 10$ ($L = 20$) model, if one fixes $\mu = 4$ and increases U_0 from 0 to 5, there would be five (ten) level crossings. Alternatively, we can say that in the L3 region (i.e., between GL2 and GL1), as U_0 increases, $\mathcal{N} = 4$ ($\mathcal{N} = 9$) states would take turn to serve as the ground states of the $L = 10$ ($L = 20$) model. As L increases, on one hand, the value of $\mathcal{N}$ would dramatically increase, and on the other hand, the span space for each of these $\mathcal{N}$ states would be greatly suppressed. In the large-L limit, the L3 region would be divided by numerous subregions where each subregion has its own ground state. Therefore, when we scan this region with a finite step (i.e., $\delta\mu = 0.01$ or $\delta U_0 = 0.01$), the system would easily jump for a subregion into other subregions, and a randomness feature in the L3 region is finally formed.

Figure 20 also suggests that the GL2 phase may have no fundamental difference from the $\mathcal{N}$ states (subregions) in the L3 region. In order to check this idea, we consider a subregion [marked as GL3 in Fig. 20(b)] in the L3 region and design a special path (i.e., $\mu = 2.7U_0 + 0.27$) connecting the SC phase and the GL3 subregion. We have calculated the nonlocality measure along this path, and the result is shown in Fig. 21. One can see that the nonlocality curve for this SC-GL3 transition is quite similar to that in the SC-GL2 transition in

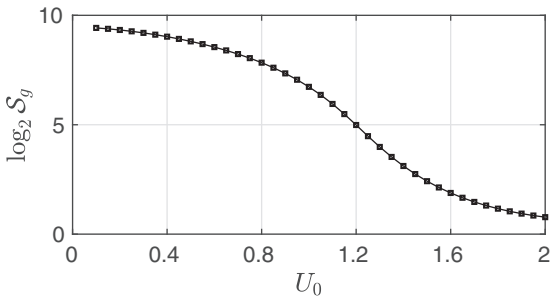

FIG. 21. Global nonlocality measure in an SC-L3 transition along a special path $\mu = 2.7U_0 + 0.27$, which connects the SC phase and the GL3 subregion in Fig. 20(b). The length of the model is $L = 20$.

Fig. 10. For instance, it first-order derivative along the path also presents a maximum.

Thereby, we conclude that the GL2 phase and the states in the L3 region belong to the same family. Consequently, we expect that previously established conclusions in the GL2 phase (for instance, the scaling behavior of the global nonlocality, the singularity of the partial nonlocality $\mathcal{S}_n$ in the SC-GL2 transition, etc.) can also be qualitatively applied in *each* subregion in the L3 region.

Finally, it needs mentioning that Fig. 20 also reveals clearly that the boundary between the SC phase and the L3 region is composed of the borders between the SC region and $\mathcal{N}$ subregions of the L3 region. In other words, this boundary is composed of $\mathcal{N}$ segments. That explains the slight random fluctuation of the SC-L3 boundary reported in the phase diagram of Fig. 15.

VIII. SUMMARY AND DISCUSSION

Previous studies on multipartite nonlocality and QPTs are mainly concentrated on uniform quantum magnetic lattices. In this paper, we have extended the study to a 1D spinless fermion quantum wire with a mixed chemical potential, i.e., $\mu_i = U_0 + \mu\cos(2\pi i\alpha)$, where U_0 and μ denote the strength of uniform and incommensurate chemical potentials, respectively. On one hand, when $\mu = 0$ this model would be reduced to the uniform model with $\mu_i = U_0$, where a topologically QPT from an SC phase to a localized phase occurs at $U_{0c} = 2$. On the other hand, when $U_0 = 0$ the model would be reduced to the incommensurate model with $\mu_i = \mu\cos(2\pi i\alpha)$, where a topological QPT occurs at $\mu_c = 2\Delta + 2$.

We have mainly considered models with $\Delta = 1$ and investigated the ground states on the μ-U_0 plane. There are four phases on the phase diagram, i.e., an SC phase and several localized regions marked as GL1, GL2, and L3. The SC phase is featured with an unambiguous zero-energy mode and a finite gap above zero energy. The GL1 phase and the GL2 phase are featured with an unambiguous energy gap and a rather narrow gap, respectively. The L3 region is featured with a strong randomness. Detailed investigations reveal that the L3 region is composed of $\mathcal{N}$ subregions. In the large-L limit, $\mathcal{N}$ would be a rather large number. Thereby, numerous states squeeze in the limited area of the L3 region. Moreover, the GL2 phase, which is reachable by tuning the parameter μ in the incommensurate model, can be regarded as an instance for these $\mathcal{N}$ states of the L3 region.

Both the SC-GL1 transitions and the SC-GL2 transition can be characterized by the global nonlocality quite well. First, the SC phase presents high nonlocality, and the localized phases present low nonlocality. Second, when the finite-size model crosses the phase boundary, the nonlocality measure would always exhibit a maximum in its first-order derivative.

We have also carried out some finite-size scaling analysis by just considering the uniform model and the incommensurate model. First, in the uniform model, the nonlocality measure scales as $\log_2 \mathcal{S}_g \sim \mathcal{K}L + b$, which has been previously observed in many translation-invariant quantum chains. In the incommensurate model where translation-invariance is broken, with some rescale technique we find that this scaling formula recovers in the large-L limit. Second, the maximum of the derivative of the nonlocality measure, which is observed in the vicinity of the critical points, tends to be quite sharp when L is large. It indicates that in the thermodynamic limit, the topological QPTs in these two models are accompanied by dramatic change of multipartite quantum correlations. It is quite reasonable that these conclusions are also valid to the general SC-GL1 transitions and the SC-GL2 transition in the mixed-potential models.

Some robustness of the topologically SC-GL1 transition in the mixed-potential model is also observed. We regard the incommensurate potential μ as a perturbation to a uniform model. When μ is small, we find that the entire $\log_2 \mathcal{S}_g \sim U_0$ curve is nearly unaffected by μ. In fact, with μ up to 0.2, the perturbed nonlocality curve and the original curve of the uniform model almost overlap each other. We suggest two causes for this robustness. First, the uniform model has a large energy gap. Second, the incommensurate perturbation may not be efficiently regarded as global perturbations. It is expected that a topological QPT would be robust against local perturbations.

Additionally, the SC-GL1 transition with fixed $\mu = 0$ (i.e., in the uniform model) and the SC-GL2 transition with $U_0 = 0$ (i.e., in the incommensurate model) have also been characterized by partial nonlocality of n-site subchains. In both situations, first, we find that the first-order derivative of $\mathcal{S}_n$ tends to be singular at the critical points, which is a strong signal for the QPTs. Second, in most regions of the topological nontrivial SC phase, the lowest rank of Bell-type inequality $\mathcal{S} \leqslant 1$ is not violated, while in the localized phases, nontrivial multipartite nonlocality is observed. Thereby, partial nonlocality for the subchains also provides us an informative perspective to characterize the QPTs.

We comment that the global nonlocality and the partial nonlocality provide a complementary characterization for the topologically nontrivial SC phase. This phase is featured with high hierarchy of global multipartite nonlocality. In contrast, in n-site subchains, the lowest rank of Bell-type inequality is not violated in most regions of the phase. The situation is similar to the n-qubit Greenberger-Horne-Zeilinger (GHZ) state $|\Psi_{\mathrm{GHZ}}\rangle = \frac{|0\rangle^{\otimes n}+|1\rangle^{\otimes n}}{\sqrt{2}}$ [57], where $|\Psi_{\mathrm{GHZ}}\rangle$ as a whole contains nontrivial multipartite quantum entanglement, but in any of its two-qubit reduced states, quantum entanglement is absent.

On the phase diagram, the most mystical region should be the L3 region. While the nonlocality measure is smooth in all other phases, it presents a multi-kink-point structure in the L3 region. The underlying mechanics is as follows. Because of the interplay between the uniform potentials and the incommensurate potentials, this region is composed of $\mathcal{N}$ subregions, and each subregion has its own ground state. We mention that in the thermodynamic limit, the value of $\mathcal{N}$ would be extremely large. All these $\mathcal{N}$ sub-regions squeeze in a limited area of the L3 region. Therefore, in the large-L limit, when we scan this region by fixing μ and changing U_0 (or fixing U_0 and changing μ), this multi-kink-point structure would evolve into some strong random fluctuations. We mention that the GL2 phase and the states in the L3 region belong to the same family. Thereby, if one can design some special paths to investigate the L3 region, it is expected that the main conclusions established in the GL2 phase would be recovered. Nevertheless, we mention that when L is large, since numerous subregions squeeze together, it may become difficult to figure out a proper path for a specific state in the L3 region.

Some issues may deserve further investigations. First, although we have considered (1) the interplay between Δ and U_0 in the uniform model and (2) the interplay between Δ and μ in the incommensurate model, the interplay between these three parameters in the mixed-potential model has not been discussed. In this complex situation, more phases may emerge and the phase diagram may be more rich. Second, although the incommensurate potential $\mu\cos(2\pi i\alpha)$ breaks the translation invariance, the cosine function itself still has a periodicity. We mention that for some quantum systems under random fields or with random interactions [58], the periodicity is completely destroyed. The performance of multipartite nonlocality in characterizing the quantum correlations and QPTs in these systems remains an open question. Third, it deserves mention that the violation of some Bell-type inequalities have been observed experimentally in Josephson phase qubits [59], photons [60], and trapped ions [61]. In particular, in Ref. [61] the violation of multipartite Bell-type inequalities in Eq. (3) with n up to 14 has been observed experimentally. How to design and carry out a Bell-type experiment on spinless fermion quantum wires would be a challenging but valuable task.

ACKNOWLEDGMENTS

We would like to express our great gratitude to the anonymous referees of this paper. The idea about considering potentials beyond the incommensurate potentials and investigating the disorder at small length scales in detail was proposed by one of the referees. The research was supported by the National Natural Science Foundation of China (Grant No. 11675124).

APPENDIX: FORMULA FOR CORRELATION FUNCTIONS

In this Appendix, we just provide the final formula for the correlation functions involved in the two-site reduced density matrix in Eq. (13) for the uniform model. For the detailed derivation process, readers are referred to original literature such as Ref. [52].

First, one shall calculate three summations over the Brillouin zone as follows,

$$a=\frac{1}{L}\sum_k \frac{\omega_k+2t\cos k+\mu}{2\omega_k},$$
$$b=\frac{1}{L}\sum_k \frac{\Delta\sin^2 k}{\omega_k},$$
$$c=\frac{1}{L}\sum_k \frac{\omega_k+2t\cos k+\mu}{2\omega_k}\cos k, \tag{A1}$$

where

$$\omega_k=\sqrt{(2t\cos k+\mu)^2+(2\Delta\sin k)^2}. \tag{A2}$$

In the thermodynamic limit, the above summation needs to be rephrased as an integral over the Brillouin zone, i.e.,

$$\lim_{L\to\infty}\frac{1}{L}\sum_k f(k)=\frac{1}{2\pi}\int_{-\pi}^{\pi} f(k)dk. \tag{A3}$$

Then, correlation functions of the fermion operators can be expressed by a, b, and c. For instance,

$$\langle c_i^\dagger c_i\rangle=a,\quad \langle c_i^\dagger c_{i+1}^\dagger\rangle=\langle c_{i+1}c_i\rangle=-b,$$
$$\langle c_i^\dagger c_{i+1}\rangle=\langle c_{i+1}^\dagger c_i\rangle=c. \tag{A4}$$

Finally, correlation functions of the spin operators can be identified readily,

$$\langle\hat\sigma_i^z\rangle=2\langle c_i^\dagger c_i\rangle-1,$$
$$\langle\hat\sigma_i^+\hat\sigma_{i+1}^+\rangle=\langle\hat\sigma_i^-\hat\sigma_{i+1}^-\rangle=\langle c_{i+1}^\dagger c_i^\dagger\rangle,$$
$$\langle\hat\sigma_i^+\hat\sigma_{i+1}^-\rangle=\langle\hat\sigma_i^-\hat\sigma_{i+1}^+\rangle=\langle c_i^\dagger c_{i+1}\rangle \tag{A5}$$

A slightly complex one is the correlation function $\langle\hat\sigma_i^z\hat\sigma_{i+1}^z\rangle$, which needs to be calculated with the help of Wick's theory as

$$\langle\hat\sigma_i^z\hat\sigma_{i+1}^z\rangle=4\langle c_i^\dagger c_i\rangle\langle c_{i+1}^\dagger c_{i+1}\rangle-4\langle c_i^\dagger c_{i+1}^\dagger\rangle\langle c_i c_{i+1}\rangle$$
$$+4\langle c_i^\dagger c_{i+1}\rangle\langle c_i c_{i+1}^\dagger\rangle-2\langle c_i^\dagger c_i\rangle-2\langle c_{i+1}^\dagger c_{i+1}\rangle+1. \tag{A6}$$

[1] S. Sachdev, *Quantum Phase Transitions* (Cambridge University Press, Cambridge, UK, 1999).
[2] S. Sachdev, Rev. Mod. Phys. **75**, 913 (2003).
[3] M. Vojta, Rep. Prog. Phys. **66**, 2069 (2003).
[4] F. D. M. Haldane, Rev. Mod. Phys. **89**, 040502 (2017).
[5] X.-G. Wen, Rev. Mod. Phys. **89**, 041004 (2017).
[6] G. F. A. Osterloh, L. Amico, and R. Fazio, Nature (London) **416**, 608 (2002).
[7] S.-J. Gu, Int. J. Mod. Phys. B **24**, 4371 (2010).
[8] J. Eisert, M. Cramer, and M. B. Plenio, Rev. Mod. Phys. **82**, 277 (2010).
[9] U. Schollwöck, Ann. Phys. **326**, 96 (2011).

[10] O. Gühne, G. Tóth, and H. J. Briegel, New J. Phys. **7**, 229 (2005).
[11] F. Levi and F. Mintert, Phys. Rev. Lett. **110**, 150402 (2013).
[12] J.-D. Bancal, C. Branciard, N. Gisin, and S. Pironio, Phys. Rev. Lett. **103**, 090503 (2009).
[13] N. Brunner, D. Cavalcanti, S. Pironio, V. Scarani, and S. Wehner, Rev. Mod. Phys. **86**, 419 (2014).
[14] N. Brunner, J. Sharam, and T. Vértesi, Phys. Rev. Lett. **108**, 110501 (2012).
[15] T. R. de Oliveira, G. Rigolin, M. C. de Oliveira, and E. Miranda, Phys. Rev. Lett. **97**, 170401 (2006).
[16] J. Batle and M. Casas, J. Phys. A: Math. Theor. **44**, 445304 (2011).
[17] D.-L. Deng, C. Wu, J.-L. Chen, S.-J. Gu, S. Yu, and C. H. Oh, Phys. Rev. A **86**, 032305 (2012).
[18] T. R. de Oliveira, A. Saguia, and M. S. Sarandy, EPL **100**, 60004 (2012).
[19] Z.-Y. Sun, Y.-Y. Wu, J. Xu, H.-L. Huang, B.-J. Chen, and B. Wang, Phys. Rev. A **88**, 054101 (2013).
[20] Z.-Y. Sun, Y.-Y. Wu, J. Xu, H.-L. Huang, B.-F. Zhan, B. Wang, and C.-B. Duan, Phys. Rev. A **89**, 022101 (2014).
[21] Z.-Y. Sun, S. Liu, H.-L. Huang, D. Zhang, Y.-Y. Wu, J. Xu, B.-F. Zhan, H.-G. Cheng, C.-B. Duan, and B. Wang, Phys. Rev. A **90**, 062129 (2014).
[22] Z.-Y. Sun, B. Guo, and H.-L. Huang, Phys. Rev. A **92**, 022120 (2015).
[23] Y. Dai, C. Zhang, W. You, Y. Dong, and C. H. Oh, Phys. Rev. A **96**, 012336 (2017).
[24] H.-G. Cheng, M. Li, Y.-Y. Wu, M. Wang, D. Zhang, J. Bao, B. Guo, and Z.-Y. Sun, Phys. Rev. A **101**, 052116 (2020).
[25] J. Bao, B. Guo, H.-G. Cheng, M. Zhou, J. Fu, Y.-C. Deng, and Z.-Y. Sun, Phys. Rev. A **101**, 012110 (2020).
[26] Z.-Y. Sun, M. Li, L.-H. Sheng, and B. Guo, Phys. Rev. A **103**, 052205 (2021).
[27] S. Campbell and M. Paternostro, Phys. Rev. A **82**, 042324 (2010).
[28] Z.-Y. Sun, M. Wang, Y.-Y. Wu, and B. Guo, Phys. Rev. A **99**, 042323 (2019).
[29] X.-Y. Feng, G.-M. Zhang, and T. Xiang, Phys. Rev. Lett. **98**, 087204 (2007).
[30] Z.-Y. Sun, M. Li, H.-X. Wen, H.-G. Cheng, J. Xu, and Y.-S. Chen,Eur. Phys. J. B **94**, 141 (2021).
[31] Z.-Y. Sun, H.-X. Wen, M. Li, and Y. Li, Phys. Rev. A **104**, 052202 (2021).
[32] F. Verstraete, J. J. García-Ripoll, and J. I. Cirac, Phys. Rev. Lett. **93**, 207204 (2004).
[33] Z.-Y. Sun, X. Guo, and M. Wang, Eur. Phys. J. B **92**, 75 (2019).
[34] J. Bao, B. Guo, Y.-H. Liu, L.-H. Shen, and Z.-Y. Sun, Phys. B: Condens. Matter **593**, 412297 (2020).
[35] Z.-Y. Sun, H.-X. Wen, M. Li, and B. Guo, Phys. Rev. A **105**, 012213 (2022).
[36] G. Roati, C. D'Errico, L. Fallani, M. Fattori, C. Fort, M. Zaccanti, G. Modugno, M. Modugno, and M. Inguscio, Nature (London) **453**, 895 (2008).
[37] A. Y. Kitaev, Phys. Usp. **44**, 131 (2001).
[38] X. Cai, L.-J. Lang, S. Chen, and Y. Wang, Phys. Rev. Lett. **110**, 176403 (2013).
[39] J.-D. Bancal, N. Brunner, N. Gisin, and Y.-C. Liang, Phys. Rev. Lett. **106**, 020405 (2011).
[40] J.-D. Bancal, J. Barrett, N. Gisin, and S. Pironio, Phys. Rev. A **88**, 014102 (2013).
[41] Q. Chen, S. Yu, C. Zhang, C. H. Lai, and C. H. Oh, Phys. Rev. Lett. **112**, 140404 (2014).
[42] J. Bowles, J. Francfort, M. Fillettaz, F. Hirsch, and N. Brunner, Phys. Rev. Lett. **116**, 130401 (2016).
[43] E. G. Cavalcanti, Q. Y. He, M. D. Reid, and H. M. Wiseman, Phys. Rev. A **84**, 032115 (2011).
[44] N. D. Mermin, Phys. Rev. Lett. **65**, 1838 (1990).
[45] A. V. Belinskiĭ and D. N. Klyshko, Phys. Usp. **36**, 653 (1993).
[46] V. Scarani and N. Gisin, J. Phys. A: Math. Gen. **34**, 6043 (2001).
[47] D. Collins, N. Gisin, S. Popescu, D. Roberts, and V. Scarani, Phys. Rev. Lett. **88**, 170405 (2002).
[48] R. F. Werner and M. M. Wolf, Phys. Rev. A **64**, 032112 (2001).
[49] B.-J. Chen, Z.-Y. Sun, H.-L. Huang, and B. Wang, Eur. Phys. J. B **87**, 282 (2014).
[50] X.-F. Qian and Z. Song, Phys. Rev. A **74**, 022302 (2006).
[51] B. Bauer, L. D. Carr, H. G. Evertz, A. Feiguin, J. Freire, S. Fuchs, L. Gamper, J. Gukelberger, E. Gull, S. Guertler, A. Hehn, R. Igarashi, S. V. Isakov, D. Koop, P. N. Ma, P. Mates, H. Matsuo, O. Parcollet, G. Pawłowski, J. D. Picon, L. Pollet, E. Santos, V. W. Scarola, U. Schollwöck, C. Silva, B. Surer, S. Todo, S. Trebst, M. Troyer, M. L. Wall, P. Werner, and S. Wessel, J. Stat. Mech. (2011) P05001.
[52] L. Elliott, S. Theodore, and D. Mattis, Ann. Phys. **16**, 407 (1961).
[53] C.-J. Shan, W.-W. Cheng, J.-B. Liu, Y.-S. Cheng, and T.-K. Liu, Sci. Rep. **4**, 4473 (2014).
[54] M. Fishman, S. R. White, and E. M. Stoudenmire, arXiv:2007.14822.
[55] I. P. McCulloch and M. Gulácsi, EPL **57**, 852 (2002).
[56] R. Horodecki, P. Horodecki, and M. Horodecki, Phys. Lett. A **200**, 340 (1995).
[57] D. M. Greenberger, M. A. Horne, and A. Zeilinger, *Bell's Theorem, Quantum Theory, and Conceptions of the Universe* (Academic Press, Dordrecht, 1989).
[58] V. Derzhko, O. Derzhko, and J. Richter, Phys. Rev. B **83**, 174428 (2011).
[59] M. Ansmann, H. Wang, R. C. Bialczak, M. Hofheinz, E. Lucero, M. Neeley, A. D. O'Connell, D. Sank, M. Weides, J. Wenner, A. N. Cleland, and J. M. Martinis, Nature (London) **461**, 504 (2009).
[60] M. Giustina, A. Mech, S. Ramelow, B. Wittmann, J. Kofler, J. Beyer, A. Lita, B. Calkins, T. Gerrits, S. W. Nam, R. Ursin, and A. Zeilinger, Nature (London) **497**, 227 (2013).
[61] B. P. Lanyon, M. Zwerger, P. Jurcevic, C. Hempel, W. Dür, H. J. Briegel, R. Blatt, and C. F. Roos, Phys. Rev. Lett. **112**, 100403 (2014).